



# Ultralow Pd bimetallic catalysts boost (de)hydrogenation for reversible H<sub>2</sub> storage

Wenjie Xue<sup>a,b</sup>, Binbin Zhao<sup>c</sup>, Hongxia Liu<sup>a,\*</sup>, Xinqing Chen<sup>d,e</sup>, Lei Liu<sup>a,\*</sup>

<sup>a</sup> School of Chemistry and Chemical Engineering, Hubei Key Laboratory of Biomass Fibers and Eco-Dyeing & Finishing Wuhan Textile University, Wuhan, Hubei 430200, China

<sup>b</sup> School of Chemistry and Chemical Engineering, Huazhong University of Science and Technology, Wuhan, Hubei 430074, China

<sup>c</sup> Department of Materials Science and Engineering National University of Singapore, Singapore 117575, Singapore

<sup>d</sup> Shanghai Advanced Research Institute, Chinese Academy of Sciences, Shanghai 201210, China

<sup>e</sup> University of Chinese Academy of Sciences, Beijing 100049, China

## ARTICLE INFO

### Keywords:

Liquid organic hydrogen carrier  
Bimetallic catalyst  
(De)hydrogenation  
N-propylcarbazole  
Density functional theory

## ABSTRACT

The facile catalytic reversible (de)hydrogenation of liquid organic hydrogen carriers (LOHC) using a single catalyst holds great value for onboard hydrogen storage. Herein, we develop a bimetallic catalyst Pd<sub>1</sub>Ni based on nonnoble metal Ni with ultralow Pd of 0.05 wt%, which enables reversible (de)hydrogenation of NPC and supports multiple cycles of reversible hydrogen uptake and release. Notably, the bimetallic catalyst Pd<sub>1</sub>Ni exhibits more excellent catalytic performance on the dehydrogenation reaction of dodecahydro-N-propylcarbazole (12H-NPC) than the 1%Pd catalyst and similar catalytic performance on the hydrogenation reaction of NPC compared to the 1%Ru catalyst. The astonishing catalytic efficiency of Pd<sub>1</sub>Ni catalysts is due to the ideal electronic structure between ultralow Pd and Ni NPs allowing rapid interfacial electron transfer to intermediates, as revealed by structural analyses and density functional theory (DFT) computations.

## 1. Introduction

Hydrogen continues to be the most promising alternative energy carrier to mitigate fossil resource depletion and environmental concerns. [1,2] Electrocatalytic water splitting driven by renewable energy sources such as solar and wind is a promising pathway for sustainable hydrogen production [3,4]. Apart from hydrogen production, hydrogen storage/transport is equally critical for the realization of hydrogen economy [5–7]. Liquid organic hydrogen carriers (LOHCs) featured by efficient storage, safe transport and successive utilization show great economic benefits for industrial applications in hydrogen storage/transport [8–12]. Among them, N-heterocycles, especially N-propylcarbazole (NPC) with high hydrogen capacity and lower operating temperature, have attracted much attention through the introduction of N atoms in carbocyclic compounds [13–15]. In fact, the key to effective storage and utilization of H<sub>2</sub> is to develop efficient catalytic systems with high performance in promoting the (de)hydrogenation reaction of N-heterocycles.

In this regard, Ru- and Rh-supported catalysts have been shown to hydrogenate N-heterocycles with excellent performance [16,17]. Pd

based noble metal catalysts have been shown to possess excellent intrinsic reactivity in the dehydrogenation of N-heterocycles [18,19]. In addition, bimetallic RuPd and RhPd catalysts have been used for reversible (de)hydrogenation reaction [20–22]. Current limitations lie in the high noble metal content, which limits its industrial applications. Therefore, there is an urgent need, but it is still a significant challenge to design a non-noble metal-based catalyst for reversible (de)hydrogenation. At present, the (de)hydrogenation reaction on transition metal catalysts has also been studied, but its poor activity and stability cannot rival noble metal catalysts [23,24]. It is well established that electron transfer exists throughout the (de)hydrogenation process between catalytic centers and substrates, which can be optimized by metal species composition to enhance catalytic activity [25–27]. For instance, transition metal bimetallic catalysts, such as Rh-Ni and Ru-Ni catalysts, exhibit exceptional hydrogenation catalytic activity, while Pd-Cu, Pd-Ni, and Pd-Cr catalysts exhibit high dehydrogenation reaction rates and selectivity [28–31]. Despite this, bifunctional transition metal catalysts that can catalyze both hydrogenation and dehydrogenation reactions are rare. There is an immediate need for affordable bifunctional catalysts capable of performing reversible (de)hydrogenation reactions

\* Corresponding authors.

E-mail addresses: [hxliu@wtu.edu.cn](mailto:hxliu@wtu.edu.cn) (H. Liu), [liulei3039@gmail.com](mailto:liulei3039@gmail.com), [leiliu@wtu.edu.cn](mailto:leiliu@wtu.edu.cn) (L. Liu).

<https://doi.org/10.1016/j.apcatb.2023.123574>

Received 12 September 2023; Received in revised form 16 November 2023; Accepted 26 November 2023

Available online 1 December 2023

0926-3373/© 2023 Elsevier B.V. All rights reserved.

to minimize resource consumption. In this regard, Ni-based catalyst with novel electronic reactivity has been explored for use in the hydrogenation of N-heterocycles [25]. Pd-based catalysts have been found to exhibit higher catalytic activity in hydrogenation reactions but lower efficiency in dehydrogenation processes [19]. In addition, Previous studies have shown that a frustrated Lewis pair consisting of a pair of  $H^-$  and  $H^+$  ions is considered to promote hydrogenation for many compounds, such as unsaturated hydrocarbons, aldehydes, carbon dioxide [32,33].  $\gamma\text{-Al}_2\text{O}_3$  with sufficient Lewis acidic, is a commonly used catalysts support in the hydrogenation of various LOHC compounds [21,22, 26,28,29]. Therefore, tuning the electronic structure of the Ni-based catalyst with ultralow Pd supported on  $\gamma\text{-Al}_2\text{O}_3$  is expected to promote electron transfer and endow it with outstandingly reversible activity in (de)hydrogenation. As such, this strategy offers a new avenue for designing non-noble metal based catalysts to enhance the efficiency of reversible hydrogenation and dehydrogenation processes, which may be a practical way for industrial applications.

Herein, a single reversible Ni-based catalyst with ultralow Pd supported on the  $\gamma\text{-Al}_2\text{O}_3$  (named  $\text{Pd}_1\text{Ni}/\gamma\text{-Al}_2\text{O}_3$ ) was developed, which is capable of efficiently catalyzing the reversible (de)hydrogenation reaction of NPC and enabling multiple cycles of reversible hydrogen adsorption and release. Notably, the bimetallic  $\text{Pd}_1\text{Ni}$  catalyst shows more excellent catalytic performances on dehydrogenation reaction of dodecahydro-NPC (12 H-NPC) with noble metal-normalized activity for  $\text{H}_2$ -Release 25 times higher than that of the dehydrogenation catalyst of  $1\%\text{Pd}/\gamma\text{-Al}_2\text{O}_3$  and similar catalytic performance on hydrogenation reaction of NPC with noble metal-normalized activity for  $\text{H}_2$ -uptake 20 times higher than that of the hydrogenation catalyst of  $1\%\text{Ru}/\gamma\text{-Al}_2\text{O}_3$ . Based on experimental results, the optimal electronic structure of the Pd atom and Ni NPs as well as the mechanism of (de)hydrogenation of NPC were investigated through density functional theory (DFT) analysis of binding energy, reaction energy profiles, and substrate molecule adsorption energies on catalyst surfaces. The introduction of ultralow levels of Pd moves the  $d$  band center of Ni to the Fermi level, improving the adsorption of reaction substrates on the catalyst, thereby enhancing catalytic activity.

## 2. Experimental section

### 2.1. Chemical and material

N-propylcarbazole (Wuhan Hechang chemical Co., Ltd.) was used as LOHC for both hydrogenation and dehydrogenation reaction; Palladium acetylacetonate ( $\text{Pd}(\text{acac})_2$ ) (Aladdin, 99%) and Nickel nitrate hexahydrate ( $\text{Ni}(\text{NO}_3)_2 \cdot 6\text{H}_2\text{O}$ ) were purchased from Aladdin; Aluminum oxide support (99%) was also from Aladdin.

### 2.2. Catalysts preparation

For the synthesis of  $\text{Pd}_1\text{Ni}/\gamma\text{-Al}_2\text{O}_3$ , 1.43 mg  $\text{Pd}(\text{acac})_2$  was mixed with 247 mg  $\text{Ni}(\text{NO}_3)_2 \cdot 6\text{H}_2\text{O}$  in 20 mL ethanol at 500 rpm for 20 min. In the next step, 1 g  $\gamma\text{-Al}_2\text{O}_3$  (Aladdin, 99%) added into the mixture. After stirring for 12 h, the water was removed at  $80^\circ\text{C}$  under stirring. For the  $\text{Pd}_1\text{Ni}$  catalyst (named  $\text{Pd}_1\text{Ni}/\gamma\text{-Al}_2\text{O}_3$ ), the loading of Pd was 0.05 wt% and the loading of Ni was 5 wt%. The same preparation of single metal catalyst with same loading, which just removes the second metal from the bimetallic catalyst. The as-prepared catalyst was reduced at  $500^\circ\text{C}$  with a heating rate of  $2^\circ\text{C}$  per minute under  $10\%\text{H}_2/\text{N}_2$  mixed gas for 3 h.

### 2.3. Catalysts characterization

Shimadzu GC-2010 Pro was used to analyze the extracted solution. An X-ray diffractometer (Rigaku, Ultima IV) with  $\text{Cu K}\alpha$  ( $\lambda = 0.154\text{ nm}$ ) radiation at a tube current of 40 mA and a voltage of 40 kV was used to measure X-ray diffraction spectra.  $\text{N}_2$  physical adsorption was

performed on the Quantachrome Autosorb-iQ2-MP nitrogen auto-sorption instrument at an adsorption temperature of  $-196^\circ\text{C}$ . The morphology and structure of the samples were tested by the ZEISS SUPRA55 SAPHIRE Field emission scanning electron microscope (FE-SEM). Ni and Pd content was measured by inductively coupled plasma-mass spectrometry Atomic Absorption Spectrometry (ICP-AES) on an iCAP-7200 plus system. A probe-corrected TEM JEM-ARM200F was used to collect HAADF-STEM images and EDS elemental mapping results. Ni K-edge measurements were conducted on the BL14W1 beam-line's XAFS station of Shanghai Synchrotron Radiation Facility. Electrochemical impedance spectroscopy (EIS) was conducted on the CHI 760E electrochemical workstation in the frequency from 0.1 Hz to 100 kHz with a signal amplitude of 5 mV at  $-0.8\text{ V}$  vs RHE in 1 M PBS ( $\text{pH}=7$ ). X-ray photoelectron spectroscopy (XPS) measurements were conducted on AXISULTRA DLD-600 W XPS from Shimadzu-Kratos Corporation (mono  $\text{Al K}\alpha$  1486.6 eV) and recorded by the hemispherical analyser with a step-size of 0.05 eV. XPS tests need to avoid exposure to air as much as possible to avoid the surface oxidation. The experiment of temperature-programmed desorption of hydrogen ( $\text{H}_2$ -TPD) was performed on a chemisorption instrument (Micromeritics ChemSorb 2950) connected to online mass spectrometry (MS, MKS Cirrus 2).

### 2.4. Catalytic tests

N-propylcarbazole (NPC) (Wuhan Hechang chemical Co., Ltd.) was used as LOHC for both hydrogenation and dehydrogenation reaction. The maximum hydrogen uptake or hydrogen release for the NPC/12 H-NPC system is 5.43 wt% calculated based on the substrate. All  $\text{H}_2$ -uptake and  $\text{H}_2$ -release values were calculated by GC and GC-MS taking all the intermediate products into account and based 5.43 wt% as 100%. For reversible hydrogen storage, the maximum hydrogen uptake is 5.43 wt %, whereas the maximum hydrogen release is up to the hydrogen uptake in the run.

General procedure for hydrogenation of NPC to 12 H-NPC. NPC (5 g 24.8 mmol) mixed with 0.5 g catalyst were added into a 100 mL stainless steel autoclave. The autoclave was flushed with hydrogen three times and a hydrogen pressure of 60 bar was adjusted. The reactor was heated to the commonly-used temperatures of  $160^\circ\text{C}$  for 1 h under magnetic stirring at 300 rpm.

General procedure for Dehydrogenation of 12 H-NPC to NPC. The 12 H-NPC was obtained by hydrogenation of NPC over the  $\text{Pd}_1\text{Ni}/\gamma\text{-Al}_2\text{O}_3$  catalyst. 12 H-NPC (5 g 24.2 mmol) mixed with 0.5 g catalyst were added into a 100 mL stainless steel autoclave. The autoclave was evacuated and flushed with argon for three times. The reactor was heated to the commonly-used temperatures of  $180^\circ\text{C}$  for 1 h under magnetic stirring at 300 rpm. Besides, the hydrogen gas was collected quantified and analysed for purity by GC.

The corresponding calculation formula is as follows:

$$\text{H}_2 \text{ Uptake ratio}(\%) = C_{\text{NPC}} \times (S_{12\text{H-NPC}} \times 1 + S_{8\text{H-NPC}} \times 0.6667 + S_{4\text{H-NPC}} \times 0.3333)$$

$$\text{H}_2 \text{ Release ratio}(\%) = C_{12\text{H-NPC}} \times (S_{\text{NPC}} \times 1 + S_{4\text{H-NPC}} \times 0.6667 + S_{8\text{H-NPC}} \times 0.3333)$$

$$\text{H}_2 \text{ Uptake rate}(\text{mL g}^{-1} \text{ min}^{-1}) = \frac{\text{H}_2 \text{ Uptake ratio} \times 5 \times 5.43\% \times 22.4 \times 1000}{M_{\text{H}_2} \times t \times m}$$

$$\text{H}_2 \text{ Release rate}(\text{mL g}^{-1} \text{ min}^{-1}) = \frac{\text{H}_2 \text{ Release ratio} \times 5 \times 5.43\% \times 22.4 \times 1000}{M_{\text{H}_2} \times t \times m}$$

$$\text{Noble metal normalized activity for } H_2 \text{ Uptake} (L \text{ g}^{-1} \text{ min}^{-1}) \\ = \frac{H_2 \text{ Uptake rate}}{w \times 1000}$$

$$\text{Noble metal normalized activity for } H_2 \text{ Release} (L \text{ g}^{-1} \text{ min}^{-1}) \\ = \frac{H_2 \text{ Release rate}}{w \times 1000}$$

C: conversion of NPC or 12 H-NPC;

S: selectivity;

t: reaction time, min;

m: mass of catalyst dosage, g;

w: noble metal loading in the catalyst;

MH<sub>2</sub>: atomic mass of H<sub>2</sub> 2 g mol<sup>-1</sup>.

## 2.5. Computational models

For the Ni catalysts, the Ni(111) surface was the most stable, which also has the most dominantly exposed crystal facets with the lowest surface energy, so it was generally chosen as the representative surface for experimental and theoretical studies. Thus, in this study, the flat Ni (111) surface was employed to investigate the dehydrogenation of 12 H-NPC to NPC, a three-layer  $p(5 \times 5)$  Ni(111) was cleaved from the the optimized lattice parameter of 3.52 Å, which was agreed with the experimental lattice parameter of 3.54 Å as shown in Fig. S1(a). From Fig. S1(a), it can be seen that the corresponding adsorption sites of Top, Hcp, Fcc and Bridge exist on the surface morphology of Ni(111). The vacuum gap was set to 15 Å to separate the slabs, which was large enough to avoid interactions between the slabs.

To probe the synergistic effect of between Pd and Ni atoms as the sites on the Pd<sub>1</sub>Ni catalysts controlling the dehydrogenation ability, for the Pd<sub>1</sub>Ni catalysts, Pd<sub>1</sub>Ni catalysts were built by replacing one Ni atom on  $p(5 \times 5)$  Ni(111) with three-layers, which was separated by a vacuum distance of 15 Å, as shown in Fig. S1(b). For Pd<sub>1</sub>Ni(111) surface, Top<sub>Ni</sub>, Top<sub>Pd</sub>, Bridge1, Bridge2, Hcp1, Hcp2, Fcc1 and Fcc2 sites exist. During the calculations, the bottom one layers was fixed at their bulk positions, whereas the top two layers and all adsorbed species were relaxed.

## 3. Results and discussion

### 3.1. Electronic structure

We investigated the geometrical and electronic structure of Ni(111) and Pd<sub>1</sub>Ni(111) with the aid of density-functional theory (DFT) calculations. Firstly, the geometrical and electronic structure of Ni(111) and Pd<sub>1</sub>Ni(111) surfaces were investigated. As plotted in Fig. 1a, each Ni atom on the pristine Ni(111) surface carries a small amount of negative charge (−0.006 e). For comparison, the Ni atoms around Pd atom were with positive charge (0.003 e) on the Pd<sub>1</sub>Ni(111) catalysts (Fig. 1b) as Pd atom with negative charge (−0.151 e), indicating that the direction of charge transfer was from Ni atoms to Pd atom. This results also evidenced that the electroactivity was located mainly on surface Pd sites and the Ni atoms played a role of electronic donor to realize bimetallic synergetic effect, which followed the order of electronegativity that Pd (2.20) is stronger than that of Ni(1.80) [34]. Meanwhile, the charge density difference of Pd<sub>1</sub>Ni(111) surfaces was well consistent with the above charge distributions analysis, which again proved that Ni atom provided the electron and more negative charges (Green and yellow represent charge depletion and accumulation) were formed around Pd atom on Pd<sub>1</sub>Ni catalysts, as shown in Fig. 1c. In addition, the introduction of Pd lengthens the metal bond length of Ni ( $d_{\text{Ni-Ni}}=2.492$  Å vs.  $d_{\text{Pd-Ni}}=2.566$  Å) (Fig. S1a,b), weakens the covalent bond, which may cause a series of changes of the adsorption energy of intermediates and the (de)hydrogenation reaction energy.

Then, the spin-polarized partial density of states (PDOS) for Ni(111) and Pd<sub>1</sub>Ni(111) were conducted to analyze electron density transfer from Ni to Pd shown in Fig. 1d-i. The *d*-band center of Ni and Pd<sub>1</sub>Ni catalysts were first investigated (Fig. 1d,g), in which the *d*-band center values of Ni(111) and Pd<sub>1</sub>Ni(111) surfaces were −1.39 and −1.46 eV, the *d*-band center of Pd<sub>1</sub>Ni(111) shifted to deeper positions (further away from the Fermi level) and became more electron-rich, confirming that the important role of Pd atoms in promoting the electron transfer. However, the *d*-band centers of bulk Pd and bulk Ni moved deeper (below the Fermi level), increasing in electron density in the process. Bulk electron transfers were effective in this electronic environment, indicating that more anti-bonding states were occupied when Pd was introduced into Ni catalysts. The *d*-band center of Pd was slightly decreased, while the valance of Ni remained stable at the surface of Pd<sub>1</sub>Ni(111). The *d*-band centers of bulk Pd and bulk Ni, on the other hand, shifted deeper (below the Fermi level), becoming more electron-rich in the process (Fig. 1f,i). The introduction of Pd into Ni catalysts may have resulted in more anti-bonding states, which can improve reaction energy, and enhance reaction kinetics. This electronic environment provided an efficient electron transfer channel for moving bulk electrons.

### 3.2. Catalyst synthesis and characterization

A range of monometallic or bimetallic catalysts were created using wet chemistry techniques, and supported with  $\gamma$ -Al<sub>2</sub>O<sub>3</sub> (Fig. 2a). Ultra-low acetylacetonate palladium are more likely to combine with free nickel ions to form bimetallic nanoparticles. The inductively coupled plasma atomic emission spectrometry (ICP-AES) was employed to determine the elemental composition of Pd (0.047 wt%) (Table S1) on the Pd<sub>1</sub>Ni/ $\gamma$ -Al<sub>2</sub>O<sub>3</sub> catalysts, which is approximately the theoretical value of 0.05 wt%. The powder XRD patterns of the different catalysts were shown in Fig. 2b and the traces of crystalline Pd and Ni cannot be found in Ni/ $\gamma$ -Al<sub>2</sub>O<sub>3</sub> and Pd<sub>1</sub>Ni/ $\gamma$ -Al<sub>2</sub>O<sub>3</sub> catalysts due to the small loading. In contrast, the crystalline Pd was detected in the 1%Pd/ $\gamma$ -Al<sub>2</sub>O<sub>3</sub> catalysts. N<sub>2</sub> sorption-desorption isotherms indicate that the Brunauer-Emmett-Teller-based specific surface area of Pd<sub>1</sub>Ni/ $\gamma$ -Al<sub>2</sub>O<sub>3</sub> is 110.2 m<sup>2</sup> g<sup>-1</sup>, which is slighter lower than that of unsupported  $\gamma$ -Al<sub>2</sub>O<sub>3</sub> (127.0 m<sup>2</sup> g<sup>-1</sup>). Furthermore, the bi-modal pore size distribution of Pd<sub>1</sub>Ni/ $\gamma$ -Al<sub>2</sub>O<sub>3</sub> remains almost unchanged at 19.9 nm after metal deposition (Fig. S2). It is widely acknowledged that single-atom catalysts can be readily synthesized and utilized at exceptionally low loadings for various reactions [35–37]. Atomic resolution high-angle annular dark-field-scanning transmission electron microscopy (HAADF-STEM) of Pd<sub>1</sub>/ $\gamma$ -Al<sub>2</sub>O<sub>3</sub> catalyst demonstrate that ultrasmall white dots are distributed throughout the whole sample, suggesting formation of atomically dispersed Pd species (Fig. S3). According to STEM image, the Pd<sub>1</sub>Ni NPs were uniformly dispersed on the  $\gamma$ -Al<sub>2</sub>O<sub>3</sub> (1.10 nm) (Fig. S4). The HADDF-STEM image of the Pd<sub>1</sub>Ni/ $\gamma$ -Al<sub>2</sub>O<sub>3</sub> catalyst reveals distinct bright dots in Fig. 2c, which correspond to the dispersed Pd single atoms highlighted in white circles. Moreover, the HADDF-STEM image (Fig. 2c) shows a lattice spacing of 0.207 nm, which is slightly longer than the lattice of Ni (111) planes of 0.203 nm, which may be attributed to the introduction of Pd atoms making the lattice of Ni-Ni bond slightly longer. The results are in good consistent with the DFT calculations (Fig. S1a,b). The corresponding elemental mapping images (Fig. 2d) demonstrate that ultrasmall green dots are distributed on the Ni NPs. Hydrogen temperature programmed reduction (H<sub>2</sub>-TPR) was then conducted to investigate the reducibility of Pd<sub>1</sub>Ni/ $\gamma$ -Al<sub>2</sub>O<sub>3</sub> and Ni/ $\gamma$ -Al<sub>2</sub>O<sub>3</sub> and further explore its structural properties [25]. Fresh Pd<sub>1</sub>Ni/ $\gamma$ -Al<sub>2</sub>O<sub>3</sub> and Ni/ $\gamma$ -Al<sub>2</sub>O<sub>3</sub> (Fig. 2e) exhibit a broad reduction peak at 200–300 °C, which can be attributed to the reduction of small NiO nanoparticles. It is worth noting that the reduction peak of fresh Pd<sub>1</sub>Ni/ $\gamma$ -Al<sub>2</sub>O<sub>3</sub> catalyst shifts to lower temperatures of 205 °C compared to Ni/ $\gamma$ -Al<sub>2</sub>O<sub>3</sub>. Such a shift has been

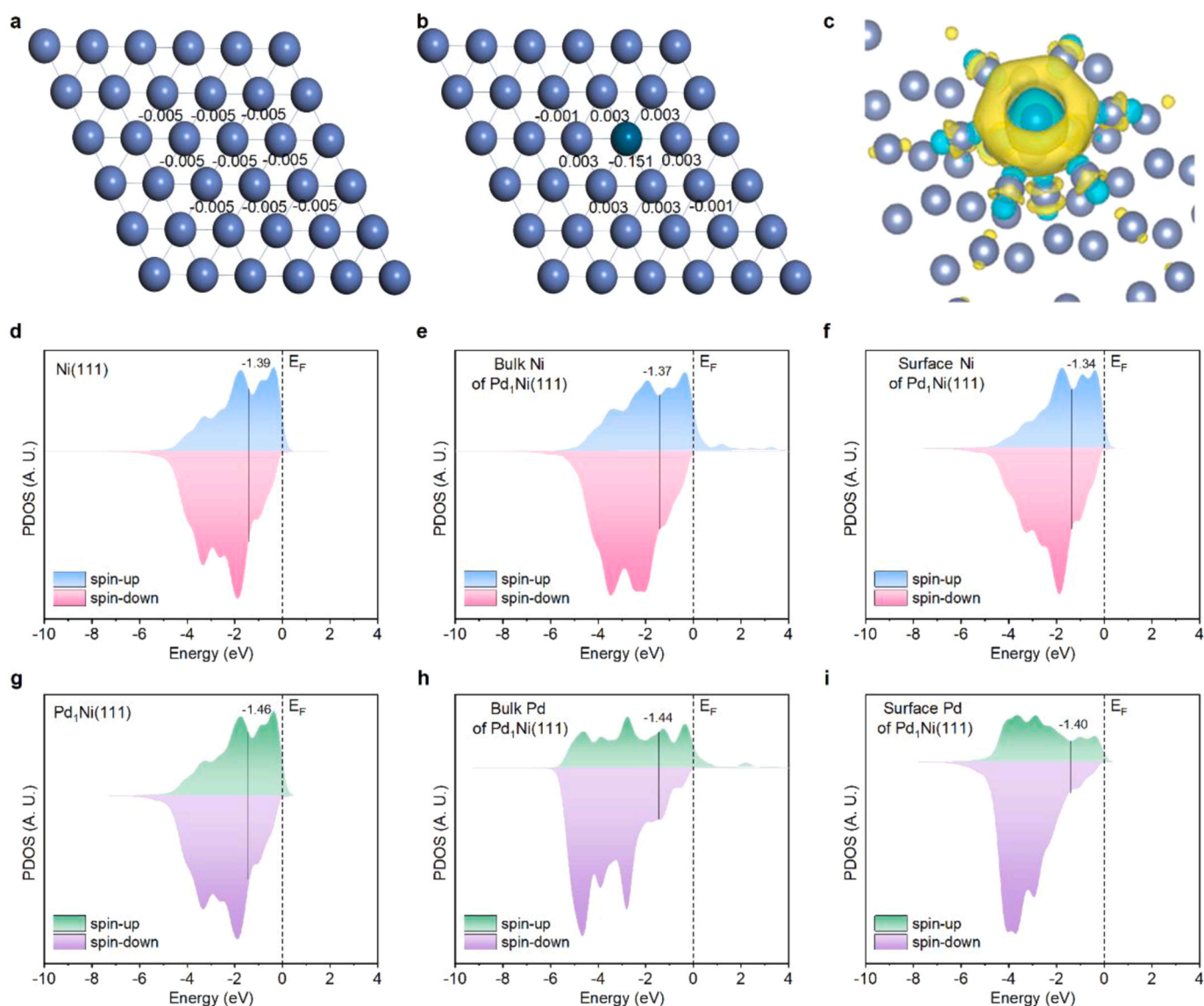


**Fig. 1.** Electronic structure of different catalysts. (a-b) The Mulliken charge distribution of Ni(111) and Pd<sub>1</sub>Ni(111), the light blue green and balls represent the Ni and Pd atoms. (c) The differential charge distribution of Pd<sub>1</sub>Ni(111), blue represents electron depletion and red represents electron enrichment, respectively and (d-i) PDOS for the surface atoms of Ni(111) and Pd<sub>1</sub>Ni(111).

previously ascribed to improved hydrogen dissociation ability for Pd<sub>1</sub>Ni/ $\gamma$ -Al<sub>2</sub>O<sub>3</sub> than Ni/ $\gamma$ -Al<sub>2</sub>O<sub>3</sub>. In addition, Ni/ $\gamma$ -Al<sub>2</sub>O<sub>3</sub> exhibited the highest reduction peak temperature of 489 °C, which implying that the Ni/ $\gamma$ -Al<sub>2</sub>O<sub>3</sub> catalyst can be reduced at 500 °C. Ex-situ X-ray absorption spectroscopy (XAS) measurements were further performed to investigate the atomic structure of porous Pd<sub>1</sub>Ni/ $\gamma$ -Al<sub>2</sub>O<sub>3</sub> catalyst [37–39]. The X-ray absorption near-edge structure (XANES) spectra given in Fig. S5 shows the comparison of Ni K-edge adsorption of the Ni/ $\gamma$ -Al<sub>2</sub>O<sub>3</sub> and Pd<sub>1</sub>Ni/ $\gamma$ -Al<sub>2</sub>O<sub>3</sub> catalysts with the reference samples of Ni foil and NiO. The white line intensity increases with ionic bonding between the nickel and oxygen increases.[39,40] The white line peak of the Ni in Ni/ $\gamma$ -Al<sub>2</sub>O<sub>3</sub> and Pd<sub>1</sub>Ni/ $\gamma$ -Al<sub>2</sub>O<sub>3</sub> catalysts was located between that of Ni foil and NiO, suggesting a valence state between the 0 and + 2 oxidation states as Ni metals are readily oxidized under ex-situ conditions. It is worth noting that Pd<sub>1</sub>Ni/ $\gamma$ -Al<sub>2</sub>O<sub>3</sub> catalysts still have higher valence states than Ni/ $\gamma$ -Al<sub>2</sub>O<sub>3</sub> catalysts under the same conditions, which is due to the charge transfer between Pd and Ni. The fourier transform (FT) EXAFS curves and the fitting structural parameters of EXAFS spectrum

[41] for Pd<sub>1</sub>Ni/ $\gamma$ -Al<sub>2</sub>O<sub>3</sub>, Ni/ $\gamma$ -Al<sub>2</sub>O<sub>3</sub>, NiO and Ni foil were presented in Fig. 2f, Fig. S6 and Table S2. It was evident that the Pd<sub>1</sub>Ni/ $\gamma$ -Al<sub>2</sub>O<sub>3</sub> exhibited a prominent coordination peak derived from the shell coordination of Ni-Ni at 2.56 Å different from that in Ni foil, NiO and Ni/ $\gamma$ -Al<sub>2</sub>O<sub>3</sub> of 2.51 Å. The Ni-Ni mean bond length of Pd<sub>1</sub>Ni/ $\gamma$ -Al<sub>2</sub>O<sub>3</sub> and Ni/ $\gamma$ -Al<sub>2</sub>O<sub>3</sub> catalysts were  $2.50 \pm 0.02$  Å and  $2.47 \pm 0.01$  Å, respectively. Compared with the Ni/ $\gamma$ -Al<sub>2</sub>O<sub>3</sub> catalysts, the longer bond length of Pd<sub>1</sub>Ni/ $\gamma$ -Al<sub>2</sub>O<sub>3</sub> may be attributed to the introduction of Pd atoms. The wavelet-transform extended X-ray absorption fine structures (WT-EXAFS) were also analyzed to examine the coordination of Pd<sub>1</sub>Ni/ $\gamma$ -Al<sub>2</sub>O<sub>3</sub> (Fig. S7). The wavelet transform signal from Pd<sub>1</sub>Ni/ $\gamma$ -Al<sub>2</sub>O<sub>3</sub> in the k range from 3 Å<sup>-1</sup> to 10 Å<sup>-1</sup> is different from those for the Ni foil, NiO and Ni/ $\gamma$ -Al<sub>2</sub>O<sub>3</sub>, which is also attributed to the introduction of Pd atoms. Based on the experimental findings, it is possible that a transfer of charges may have taken place, resulting in a shift in the surface electronic structure to pure Pd (Fig. 1). This is in line with the calculated discrepancy in charge density difference. In addition, the electronic interaction between Pd and Ni was revealed by X-ray photoemission



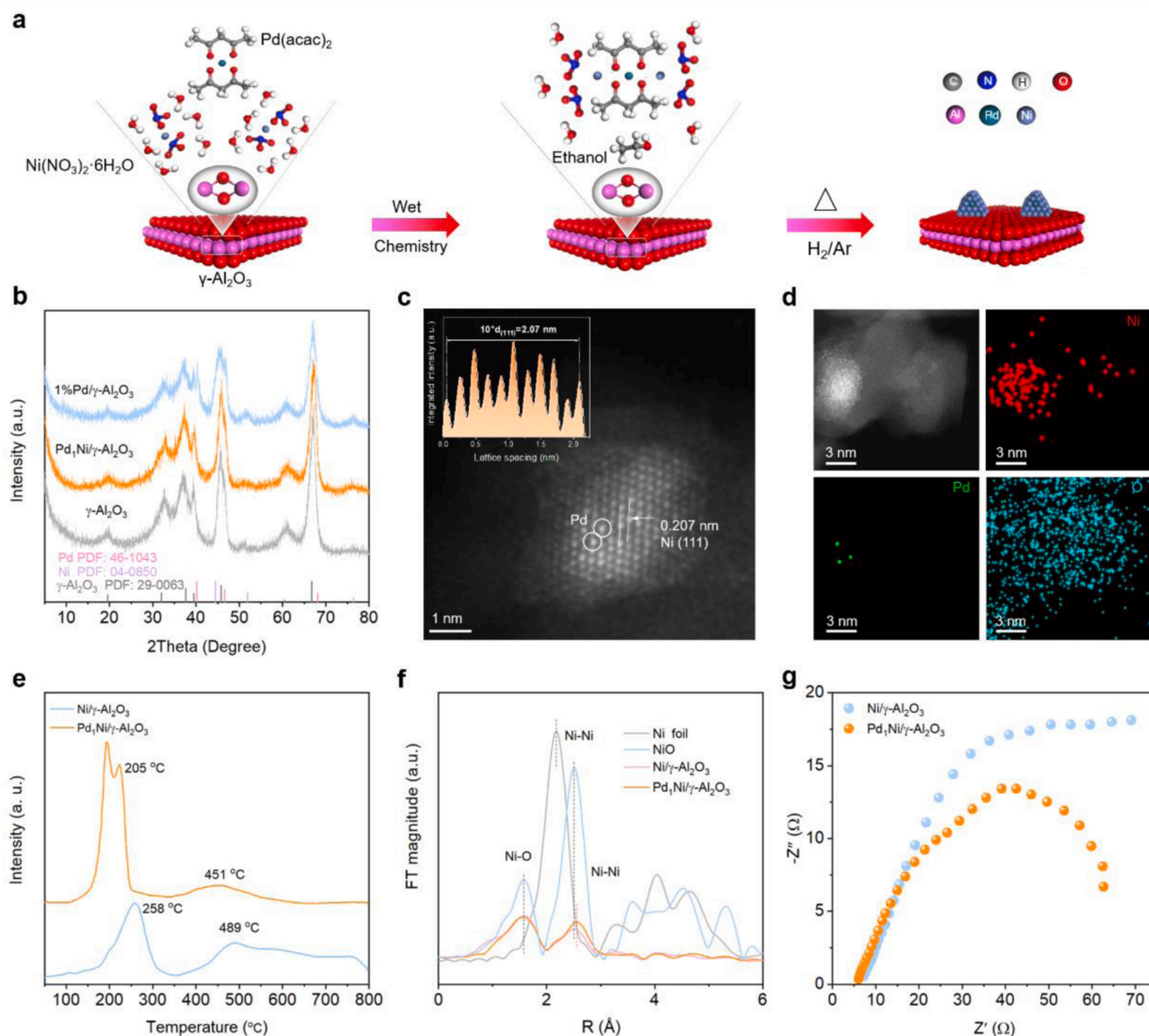


**Fig. 2.** Characterization. (a) Schematic illustration of synthesis of Pd<sub>1</sub>Ni/γ-Al<sub>2</sub>O<sub>3</sub> bimetallic catalysts. (b) XRD pattern of the Pd<sub>1</sub>Ni/γ-Al<sub>2</sub>O<sub>3</sub>, 1%Pd/γ-Al<sub>2</sub>O<sub>3</sub> and γ-Al<sub>2</sub>O<sub>3</sub> samples. (c) HAADF-STEM image of Pd<sub>1</sub>Ni/γ-Al<sub>2</sub>O<sub>3</sub> catalysts. (d) STEM and the corresponding elemental mapping images of Pd<sub>1</sub>Ni/γ-Al<sub>2</sub>O<sub>3</sub> catalysts. (e) H<sub>2</sub>-TPR patterns of Pd<sub>1</sub>Ni/γ-Al<sub>2</sub>O<sub>3</sub> and Ni/γ-Al<sub>2</sub>O<sub>3</sub> with temperatures from 50° to 800 °C. (f) FT k<sub>2</sub>-weighted EXAFS spectra of the Ni/γ-Al<sub>2</sub>O<sub>3</sub> and Pd<sub>1</sub>Ni/γ-Al<sub>2</sub>O<sub>3</sub> catalysts with the reference samples of Ni foil and NiO. (g) EIS results of Pd<sub>1</sub>Ni/γ-Al<sub>2</sub>O<sub>3</sub> and Ni/γ-Al<sub>2</sub>O<sub>3</sub> catalysts.

spectroscopy (XPS) studies in the Ni 2p and Pd 3d region (Fig. S8). The Ni 2p XPS spectra of both catalysts show peaks near the 2p<sub>3/2</sub> of Ni<sup>0</sup> binding energy of 853.2 eV. We found that the charge transfer between Pd and Ni caused a significant positive binding energy shift of Ni<sup>0</sup> 2p for the Pd<sub>1</sub>Ni/γ-Al<sub>2</sub>O<sub>3</sub> sample of 0.6 eV compared to Ni/γ-Al<sub>2</sub>O<sub>3</sub>. Notably, Ni generally presents an oxidized state in XPS characterization testing due to Ni catalysts are more sensitive to deactivation by air and other oxidizers [42–44]. Therefore, The Pd K-edge XANES and Pd 3d XPS spectra show the poor signal strength of Pd<sub>1</sub>Ni/γ-Al<sub>2</sub>O<sub>3</sub> sample because of ultralow content of Pd (Fig. S9,10). Then, the electrochemical impedance spectroscopy (EIS) results (Fig. 2g) demonstrated that Nyquist plots diameter for Pd<sub>1</sub>Ni/γ-Al<sub>2</sub>O<sub>3</sub> was observed to be lower compared with that of Ni/γ-Al<sub>2</sub>O<sub>3</sub>, meaning electron transfer of Pd<sub>1</sub>Ni/γ-Al<sub>2</sub>O<sub>3</sub> was faster than that of Ni/γ-Al<sub>2</sub>O<sub>3</sub>. These results further confirm the existence of the charge transfer between Pd and Ni.

### 3.3. Catalytic performance

The unique Pd<sub>1</sub>Ni/γ-Al<sub>2</sub>O<sub>3</sub> catalyst may become a versatile catalyst appropriate for reversible (de)hydrogenation reactions of NPC due to the strong electrochemical contact between bimetallic Ni and Pd species (Fig. 3a). Thus, in a batch reactor (Fig. S11), reversible (de)hydrogenation reactions were examined with the use of a bimetallic catalyst composed of Pd<sub>1</sub>Ni/γ-Al<sub>2</sub>O<sub>3</sub>, monometallic Pd<sub>1</sub>/γ-Al<sub>2</sub>O<sub>3</sub> and Ni/γ-Al<sub>2</sub>O<sub>3</sub> catalysts. and gas chromatography (GC) measurements were employed to calculate the absorption and release of hydrogen. As we know, supported Ru and Pd catalysts show excellent hydrogenation and dehydrogenation performance of N-heterocycles respectively [16–22]. In order to better evaluate the performance of our catalyst, Ru and Pd based catalysts with the loading of 1% were employed for comparison. The dehydrogenation reaction of 12 H-NPC was initially assessed at commonly-used temperatures of 180 °C over a period of 1 h (Fig. 3b).

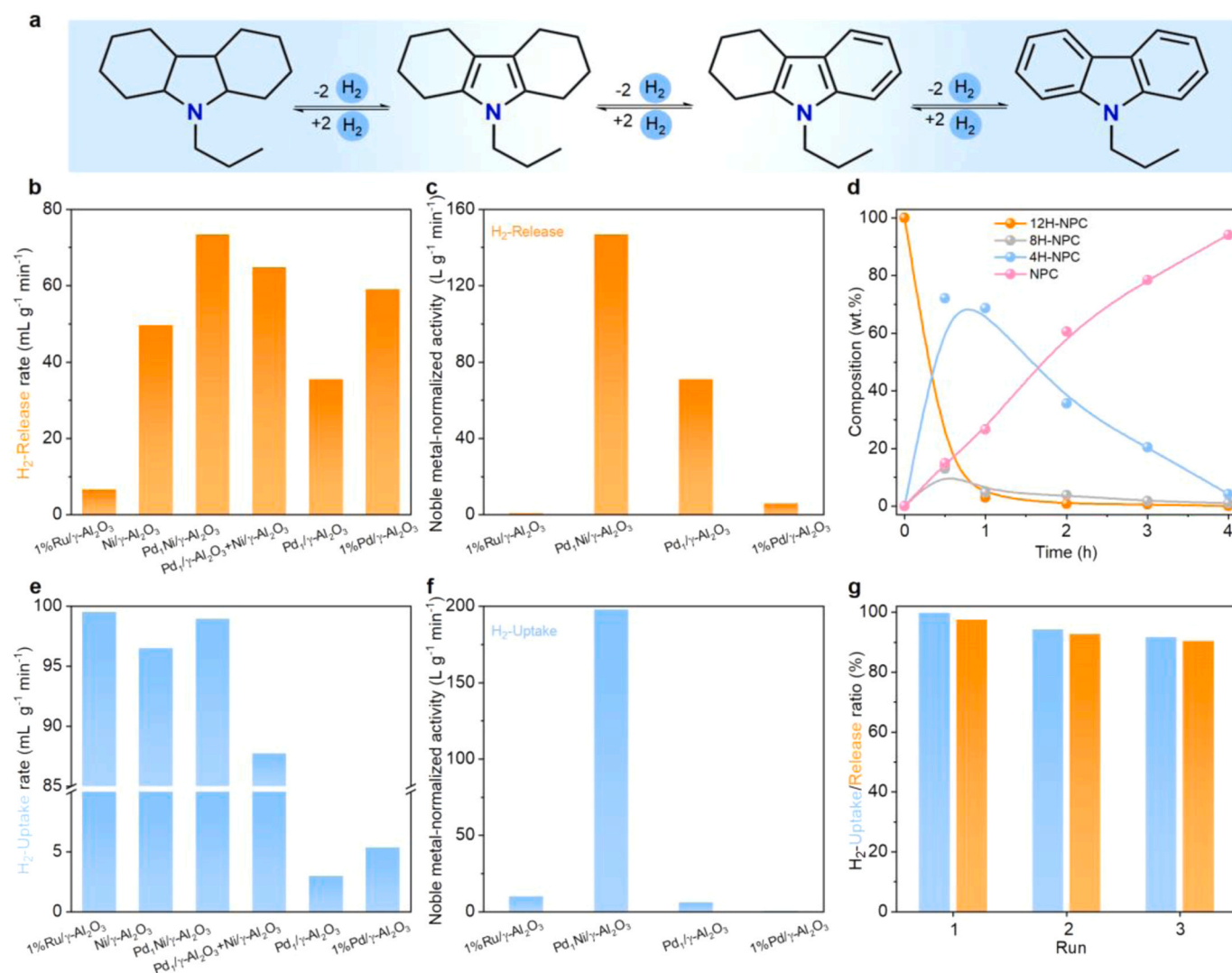


**Fig. 3.** Catalytic performance comparison for (de)hydrogenation. (a) the plausible reaction paths of (de)hydrogenation of NPC. (b) Dehydrogenation of 12 H-NPC on different catalysts. 180 °C, 1 h, 5.0 g reactant, 0.5 g catalyst. (c) Noble metal-normalized activity for H<sub>2</sub>-Release based on the dehydrogenation of 12 H-NPC on different noble metal catalysts. (d) Time-dependent product distribution in the dehydrogenation of 12 H-NPC over Pd<sub>1</sub>Ni/γ-Al<sub>2</sub>O<sub>3</sub>. 180 °C, 5.0 g reactant, 0.5 g catalyst. (e) Hydrogenation of NPC on Pd<sub>1</sub>Ni/γ-Al<sub>2</sub>O<sub>3</sub> catalysts on different catalysts. P(H<sub>2</sub>) = 60 bar, 5 g reactants, 0.5 g catalyst, 1 h. (f) Noble metal-normalized activity for H<sub>2</sub>-Uptake based on the hydrogenation of NPC on different noble metal catalysts. (d) Catalyst reusability test: 0.5 g catalyst, 5.0 g N-ethylcarbazole, hydrogenation: P(H<sub>2</sub>) = 60 bar, 5 g reactant, 0.5 g catalyst, 2 h; dehydrogenation: 180 °C, 5.0 g reactant, 0.5 g catalyst, 6 h.

The Pd<sub>1</sub>Ni/γ-Al<sub>2</sub>O<sub>3</sub> catalysts demonstrate excellent catalytic efficiency on dehydrogenation with hydrogen release rate of 73.4 mL g<sup>-1</sup> min<sup>-1</sup> for 12 H-NPC than the monometallic Pd<sub>1</sub>/γ-Al<sub>2</sub>O<sub>3</sub> catalysts (35.5 mL g<sup>-1</sup> min<sup>-1</sup>) and monometallic Ni/γ-Al<sub>2</sub>O<sub>3</sub> catalysts (49.7 mL g<sup>-1</sup> min<sup>-1</sup>). As compared with the standard dehydrogenation catalyst of 1%Pd/γ-Al<sub>2</sub>O<sub>3</sub> (59.0 mL g<sup>-1</sup> min<sup>-1</sup>), the Pd<sub>1</sub>Ni/γ-Al<sub>2</sub>O<sub>3</sub> catalysts exhibited significantly enhanced catalytic performance towards the dehydrogenation of 12 H-NPC. Another sample of physical mixture Ni/γ-Al<sub>2</sub>O<sub>3</sub> and Pd<sub>1</sub>/γ-Al<sub>2</sub>O<sub>3</sub> was also examined for comparison to rule out the possibility that electronic interactions in Pd<sub>1</sub>Ni/γ-Al<sub>2</sub>O<sub>3</sub> catalysts contributed to our desired improvement in dehydrogenation. As illustrated in Fig. 3b, the corresponding rate of hydrogen release for 12H-NPC using a physical mixture of Ni/γ-Al<sub>2</sub>O<sub>3</sub> and Pd<sub>1</sub>/γ-Al<sub>2</sub>O<sub>3</sub> catalysts is 64.8 mL g<sup>-1</sup> min<sup>-1</sup>, which is inferior to that of the Pd<sub>1</sub>Ni/γ-Al<sub>2</sub>O<sub>3</sub> catalyst (73.4 mL g<sup>-1</sup> min<sup>-1</sup>). Next, the noble metal-normalized activity was calculated which based on the release rate of H<sub>2</sub> from the dehydrogenation of 12 H-NPC normalized over the total noble metal loading, showing the catalytic power of the catalyst based on all loaded noble metal (Fig. 3c), an important economic measure of noble metal catalysts.

Clearly, Pd<sub>1</sub>Ni/γ-Al<sub>2</sub>O<sub>3</sub> catalysts exhibits the highest H<sub>2</sub>-release activity of 146.8 L<sup>-1</sup> g<sup>-1</sup> min<sup>-1</sup> among all catalysts, with 2 times higher than that of the Pd<sub>1</sub>/γ-Al<sub>2</sub>O<sub>3</sub> catalysts (71.0 L<sup>-1</sup> g<sup>-1</sup> min<sup>-1</sup>) and 25 times higher than that of the dehydrogenation catalyst of 1%Pd/γ-Al<sub>2</sub>O<sub>3</sub> (5.9 L<sup>-1</sup> g<sup>-1</sup> min<sup>-1</sup>), which is attributed to the electronic interactions between the Pd single atom and Ni NPs in the Pd<sub>1</sub>/γ-Al<sub>2</sub>O<sub>3</sub> catalysts. According to Sabatier principle [45], the interplay between reactants, intermediates and the surface of the catalyst directly influences the catalytic activity of heterogeneous catalysts. Thus, the distribution of all intermediates and products with respect to reaction time was studied (Fig. 3d). This means that as soon as the reaction began over Pd<sub>1</sub>Ni/γ-Al<sub>2</sub>O<sub>3</sub> catalysts, 12 H-NPC was rapidly consumed. Tetrahydro-N-propylcarbazole (4H-NPC) and octahydro-N-propylcarbazole (8H-NPC) successfully created intermediate products that successfully achieved their maximum value. The conversion from 8H-NPC to 4H-NPC was also found to be fast over Pd<sub>1</sub>Ni/γ-Al<sub>2</sub>O<sub>3</sub> catalysts. Afterwards, both 4H-NPC and 8H-NPC were consumed and the fully hydrogenated product NPC was achieved eventually. However, the production of NPC from 4H-NPC is rather slow, indicating that 4H-NPC appears to be a kinetically stable

intermediate in 12H-NPC dehydrogenation over  $\text{Pd}_1\text{Ni}/\gamma\text{-Al}_2\text{O}_3$  catalysts, which is in agreement with previous work [21]. In addition,  $\text{H}_2$  was collected, measured, and subjected to GC purity analysis (Fig. S12).

The hydrogenation reaction was then evaluated within 1 h at a common temperature of  $160^\circ\text{C}$  (Fig. 3e). Surprisingly,  $\text{Pd}_1\text{Ni}/\gamma\text{-Al}_2\text{O}_3$  catalysts exhibit higher performance with  $\text{H}_2$  uptake rate ( $99.0 \text{ mL g}^{-1} \text{ min}^{-1}$ ) for NPC than the monometallic  $\text{Pd}_1/\gamma\text{-Al}_2\text{O}_3$  catalysts ( $3.0 \text{ mL g}^{-1} \text{ min}^{-1}$ ) and monometallic  $\text{Ni}/\gamma\text{-Al}_2\text{O}_3$  catalysts ( $96.5 \text{ mL g}^{-1} \text{ min}^{-1}$ ). Importantly, the  $\text{Pd}_1\text{Ni}/\gamma\text{-Al}_2\text{O}_3$  catalysts exhibited comparable catalytic performance to that of standard hydrogenation catalyst of  $1\%\text{Ru}/\gamma\text{-Al}_2\text{O}_3$  ( $99.5 \text{ mL g}^{-1} \text{ min}^{-1}$ ). The  $\text{Pd}/\gamma\text{-Al}_2\text{O}_3$  catalysts demonstrate superior efficiency on dehydrogenation of 12 H-NPC, while the hydrogenation of NPC is unfavorable, with a hydrogen uptake ratio of  $5.3 \text{ mL g}^{-1} \text{ min}^{-1}$ . Similarly, the  $\text{Pd}_1\text{Ni}/\gamma\text{-Al}_2\text{O}_3$  catalysts demonstrate superior dehydrogenation performance compared to a physical mixture of  $\text{Pd}_1/\gamma\text{-Al}_2\text{O}_3$  and  $\text{Ni}/\gamma\text{-Al}_2\text{O}_3$  catalysts ( $87.7 \text{ mL g}^{-1} \text{ min}^{-1}$ ). Next, the noble metal-normalized activity was calculated based on the uptake rate of  $\text{H}_2$  through the hydrogenation NPC normalized over the total noble metal loading, showing the hydrogenation catalytic power of the catalyst based on all loaded noble metal (Fig. 3f). Clearly,  $\text{Pd}_1\text{Ni}/\gamma\text{-Al}_2\text{O}_3$  catalysts exhibits the highest noble metal-normalized activity for  $\text{H}_2$ -uptake of  $197.9 \text{ L}^{-1} \text{ g}^{-1} \text{ min}^{-1}$  among all catalysts, with normalized activity 20 times higher than that of the hydrogenation catalyst of  $1\%\text{Ru}/\gamma\text{-Al}_2\text{O}_3$  ( $9.9 \text{ L g}^{-1} \text{ min}^{-1}$ ). The monometallic  $1\%\text{Pd}/\gamma\text{-Al}_2\text{O}_3$  catalysts are almost inactive for the hydrogenation of NPC. The

monometallic  $\text{Ni}/\gamma\text{-Al}_2\text{O}_3$  catalysts have superior catalytic hydrogenation activity but with poor catalytic dehydrogenation activity. In addition to being more effective at dehydrogenating 12 H-NPC reactions, the  $\text{Pd}_1\text{Ni}/\gamma\text{-Al}_2\text{O}_3$  bimetallic catalysts also exhibit improved catalytic activity for NPC hydrogenation processes. In addition, the lower catalytic activity and selectivity over a physical mixture of  $\text{Pd}_1/\gamma\text{-Al}_2\text{O}_3$  and  $\text{Ni}/\gamma\text{-Al}_2\text{O}_3$  in comparison to that of  $\text{Pd}_1\text{Ni}/\gamma\text{-Al}_2\text{O}_3$  undoubtedly exhibit that the improved (de)hydrogenation performance of NPC is mainly ascribed to electronic interactions between the Pd atom and the Ni NPs in the  $\text{Pd}_1\text{Ni}/\gamma\text{-Al}_2\text{O}_3$  catalysts, which is also evidenced by DFT computations and structural analyses. An in-depth overview of product distribution can be found in Table S3.4. Notably, the  $\text{Pd}_1\text{Ni}/\gamma\text{-Al}_2\text{O}_3$  catalysts exhibited more excellent or comparable catalytic performance than the previously reported noble metal catalysts with higher loading capacity (Table S5). In addition, the reactivity of  $\text{Pd}_1\text{Ni}/\gamma\text{-Al}_2\text{O}_3$  catalysts was investigated, and after repeating this process three times, there was minimal reduction in the storage capacity of hydrogen. (Fig. 3g). It should be pointed out that catalysts need to avoid exposure to air as much as possible to avoid significant performance losses (Fig. S13).

### 3.4. DFT calculation

Based on the structural analysis and experimental results, the dehydrogenation reaction of 12 H-NPC on  $\text{Ni}(111)$  and  $\text{Pd}_1\text{Ni}(111)$  were investigated. Note that electrostatic potential (ESP) of the van der Waals

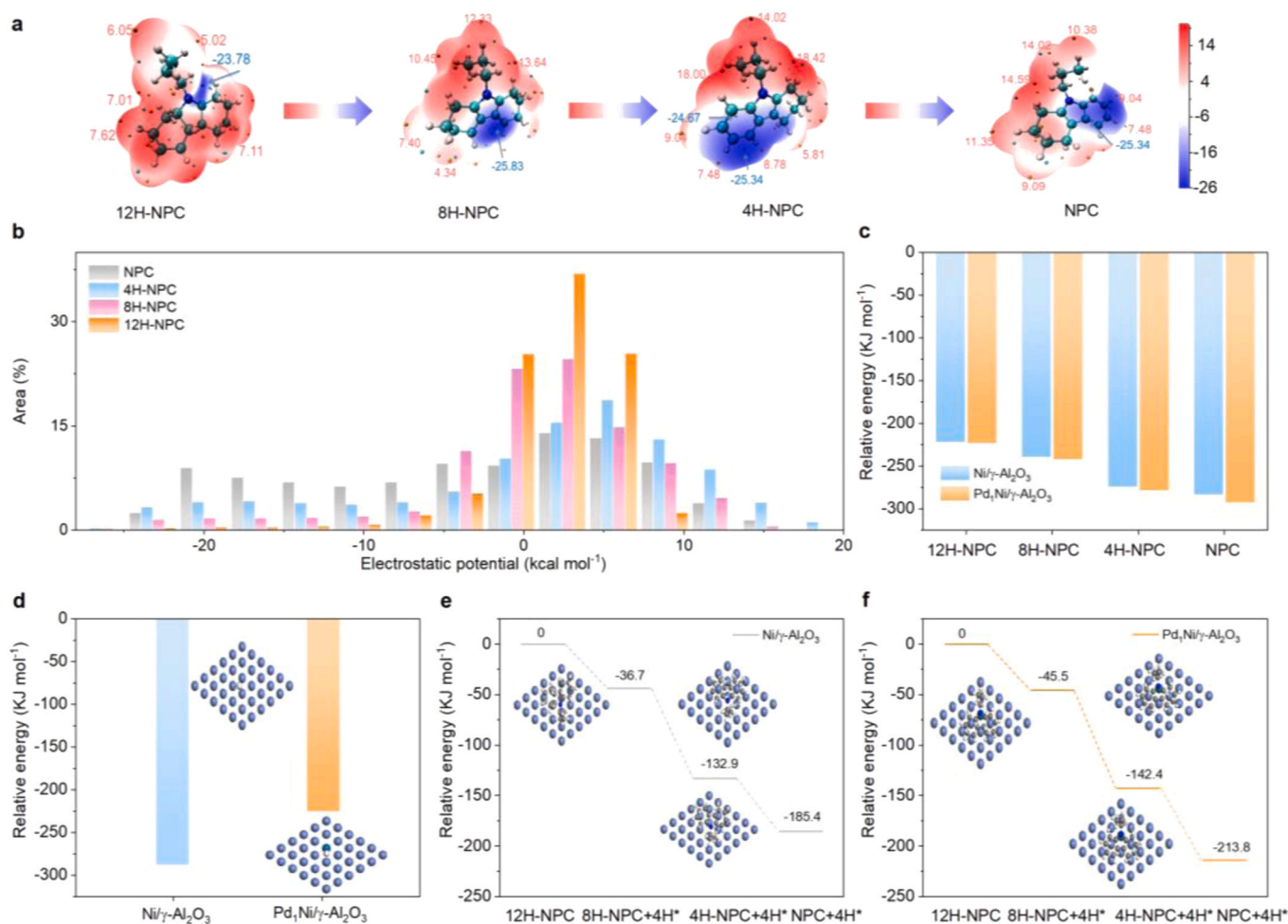


**Fig. 4.** (a, b) ESP color maps and the surface area distribution of the ESP on the isolated 12 H-NPC, 8 H-NPC, 4 H-NPC and NPC. (c) Adsorption energy for related intermediates on the  $\text{Ni}(111)$  and  $\text{Pd}_1\text{Ni}(111)$  surfaces. (d) Adsorption energy for  $\text{H}^*$  on the  $\text{Ni}(111)$  and  $\text{Pd}_1\text{Ni}(111)$  surfaces. (e, f) The dehydrogenation of 12 H-NPC to NPC on the  $\text{Ni}(111)$  and  $\text{Pd}_1\text{Ni}(111)$  surfaces.



(vdW) surface is closely related to adsorption energy. In order to analyze the electrostatic potential distribution, the vdW surface mapped by ESP (Fig. 4a) and the associated area distribution of various ESP intervals (Fig. 4b) were classified to study the electrostatic potential distribution of 12 H-NPC, 8 H-NPC, 4 H-NPC and NPC. The positive or negative increase of ESP as the red or the blue area becomes darker (Fig. 4a). The negatively increase of ESP mapped vdW surfaces along with the dehydrogenation of 12 H-NPC into 8 H-NPC, 4 H-NPC and NPC is largely attributable to the obviously negative charges of  $\pi$  electrons on aromatic rings (Fig. 4b). From an electrostatic perspective, aromatic rings will be simpler to adsorb due to their higher negative electron cloud density. Then, the adsorption of nH-NPC ( $n = 0, 4, 8$  and 12) and  $H^*$  on Ni(111) and Pd<sub>1</sub>Ni(111) were studied, as shown in Fig. 4c,d and Fig. S14,15. For nH-NPC ( $n = 0, 4, 8$  and 12), the adsorption energy was improved along with the dehydrogenation of 12H-NPC into 8H-NPC, 4H-NPC and NPC whether on Ni(111) or Pd<sub>1</sub>Ni(111), which is largely owing to the increase negative electron cloud density of the aromatic rings. Compared with pure Ni(111), the adsorption energy of nH-NPC ( $n = 0, 4, 8$  and 12) on the Pd<sub>1</sub>Ni(111) catalysts was improved especially with the dehydrogenation of 12H-NPC into 8H-NPC, 4H-NPC and NPC, which is largely due to that the positive charge of Ni atoms around Pd atom is easier to absorb negative electron cloud density of the aromatic rings. In addition, the adsorption energy of  $H^*$  on Pd<sub>1</sub>Ni(111) of  $-224.6 \text{ kJ}\cdot\text{mol}^{-1}$  is lower than it on Ni(111) of  $-287.5 \text{ kJ}\cdot\text{mol}^{-1}$  given that the positive charge of Ni atoms around Pd atom is harder to absorb  $H^*$ , which means that the  $H^*$  is easier to be removed and it is beneficial for dehydrogenation. It is worth noting that the introduction of Pd atom to Ni(111) enhances the adsorption of dehydrogenation products and reduces the adsorption of  $H^*$ , resulting in better catalytic performance for dehydrogenation. It is evident that the addition of Pd affects the electronic characteristics rather than the ensemble geometry, as well as the number of transfer electrons and binding energy. It was also believed that the binding energy was directly influenced by the  $d$ -band center. [46,47].

Furthermore, the Gibbs free energy ( $\Delta G \text{ kJ}\cdot\text{mol}^{-1}$ ) of dehydrogenation process from 12 H-NPC to 8 H-NPC, 4 H-NPC and NPC on Ni(111) and Pd<sub>1</sub>Ni(111) surfaces were carried out to evaluate the underlying reaction mechanism. As displayed in Fig. 4e, the dehydrogenation processes on the Ni(111) catalysts were all exothermic with reaction energies of  $-36.7$ ,  $-92.2$  and  $-52.8 \text{ kJ}\cdot\text{mol}^{-1}$ . For comparison, the dehydrogenation processes of 12 H-NPC to NPC on Pd<sub>1</sub>Ni(111) catalysts were also all exothermic with reaction energies of  $-45.5$ ,  $-96.9$  and  $-71.4 \text{ kJ}\cdot\text{mol}^{-1}$  (Fig. 4 f). On condition that the total Gibbs free energy from 12H-NPC to NPC on Pd<sub>1</sub>Ni(111) is lower to that on Ni(111), this result indicates that Pd<sub>1</sub>Ni(111) catalysts were more in favor of dehydrogenation. In addition, the dehydrogenation process from 4H-NPC to NPC was considered as the rate-limiting step evidenced by our experiments and previous studies. The Gibbs free energy of dehydrogenation process from 4H-NPC to NPC is  $-71.4 \text{ kJ}\cdot\text{mol}^{-1}$ , lower than that on Ni(111) catalysts of  $-52.8 \text{ kJ}\cdot\text{mol}^{-1}$ . The above analysis confirm that the outstanding catalytic performance of Pd<sub>1</sub>Ni(111) catalysts in dehydrogenation reactions, which is largely attributable to the introduction of Pd atoms changes the electronic environment around Ni atoms, further causing the synergistic effect between Pd and Ni atoms. The DFT computations are consistent with our experimental findings.

#### 4. Conclusion

In conclusion, a single reversible Pd<sub>1</sub>Ni/ $\gamma$ -Al<sub>2</sub>O<sub>3</sub> bimetallic catalyst with ultralow Pd of 0.05 wt% utilized to (de)hydrogenate of NPC was successfully synthesized for the hydrogen storage and release. The as synthesized Pd<sub>1</sub>Ni/ $\gamma$ -Al<sub>2</sub>O<sub>3</sub> catalysts show an effectively reversible activity and enables several cycles of reversible hydrogen uptake and release. Notably, the bimetallic Pd<sub>1</sub>Ni catalyst shows more excellent catalytic performances on dehydrogenation reaction of dodecahydro-NPC (12H-NPC) with noble metal-normalized activity for H<sub>2</sub>-Release 25 times higher than that of the dehydrogenation catalyst of 1%Pd/

$\gamma$ -Al<sub>2</sub>O<sub>3</sub> and similar catalytic performance on hydrogenation reaction of NPC with noble metal-normalized activity for H<sub>2</sub>-uptake 20 times higher than that of the hydrogenation catalyst of 1%Ru/ $\gamma$ -Al<sub>2</sub>O<sub>3</sub>. The ideal electronic structure between ultralow Pd and Ni NPs could shed light on the advantageous processes for the hydrogenation and dehydrogenation on Pd<sub>1</sub>Ni/ $\gamma$ -Al<sub>2</sub>O<sub>3</sub>. To determine the ideal electronic structure between ultralow Pd and Ni NPs and the probable mechanism of the hydrogenate of NPC and dehydrogenate of 12H-NPC, DFT analysis of the binding energy between Pd and Ni, reaction energy profiles, and adsorption energies of substrate molecules on the catalytic surface was performed. The introduction of the Pd atom raises Ni's valence state, moves Ni's  $d$ -band center to the Fermi level, and improves the adsorption, reaction energy and kinetics, which thus further improved the catalytic performance.

#### CRediT authorship contribution statement

**Wenjie Xue:** Experimental, Characterization, Writing – original-review. **Binbin Zhao:** Experimental, Characterization. **Hongxia Liu:** DFT calculation, Conceptualization, Investigation, Methodology, Formal analysis, Funding acquisition, Writing – review & editing. **Xinqing Chen:** Supervision, Methodology, Funding acquisition. **Lei Liu:** Investigation, Methodology, Formal analysis, Supervision.

#### Declaration of Competing Interest

The authors declare the following financial interests/personal relationships which may be considered as potential competing interests:

#### Data availability

No data was used for the research described in the article.

#### Acknowledgements

The authors acknowledge financial supports from National Key Research and Development Program of China (2022YFE0208300), Natural Science Foundation of China (22078354, 21776295) and the Opening Project of Hubei Key Laboratory of Biomass Fibers and Eco-Dyeing & Finishing (No. 223009027). Thanks to eceshi ([www.eceshi.com](http://www.eceshi.com)) for H<sub>2</sub>-TPR test.

#### Appendix A. Supporting information

Supplementary data associated with this article can be found in the online version at doi:10.1016/j.apcatb.2023.123574.

#### References

- [1] T. He, P. Pachfule, H. Wu, Q. Xu, P. Chen, Hydrogen carriers, Nat. Rev. Mater. 1 (2016) 1–17.
- [2] L. Schlögl, A. Züttel, Hydrogen-storage materials for mobile applications, Nature 414 (2001) 353–358.
- [3] J. Wang, H. Yang, F. Li, L. Li, J. Wu, S. Liu, T. Cheng, Y. Xu, Q. Shao, X. Huang, Single-site Pt-doped RuO<sub>2</sub> hollow nanospheres with interstitial C for high-performance acidic overall water splitting, Sci. Adv. 8 (2022) 1–11.
- [4] H. Dotan, A. Landman, S. Sheehan, K. Malviya, G. Shter, G. Grader, Decoupled hydrogen and oxygen evolution by a two-step electrochemical-chemical cycle for efficient overall water splitting, Nat. Energy 4 (2019) 786.
- [5] C. Dong, Z. Gao, Y. Li, M. Peng, M. Wang, D. Ma, Fully exposed palladium cluster catalysts enable hydrogen production from nitrogen heterocycles, Nat. Catal. 5 (2022) 485–493.
- [6] M. Niermann, S. Drünert, M. Kaltschmitt, K. Bonhoff, Liquid organic hydrogen carriers (LOHCs)-techno-economic analysis of LOHCs in a defined process chain, Energy Environ. Sci. 12 (2019) 290–307.
- [7] D. Mellmann, P. Sponholz, H. Junge, M. Beller, Formic acid as a hydrogen storage material-development of homogeneous catalysts for selective hydrogen release, Chem. Soc. Rev. 45 (2016) 3954–3988.
- [8] Y. Zou, N. von Wolff, A. Anaby, D. Milstein, Ethylene glycol as an efficient and reversible liquid-organic hydrogen carrier, Nat. Catal. 2 (2019) 415–422.



- [9] A. Boddien, D. Mellmann, F. Gärtner, R. Jackstell, H. Junge, P. Dyson, M. Beller, Ethylene glycol as an efficient and reversible liquid-organic hydrogen carrier, *Science* 333 (2011) 1733–1736.
- [10] J. Hull, Y. Himeda, W. Wang, B. Hashiguchi, R. Periana, D. Szalda, E. Fujita, Reversible hydrogen storage using CO<sub>2</sub> and a proton-switchable iridium catalyst in aqueous media under mild temperatures and pressures, *Nat. Chem.* 4 (2012) 383–388.
- [11] C. Gunanathan, Y. Ben-David, D. Milstein, Direct synthesis of amides from alcohols and amines with liberation of H<sub>2</sub>, *Science* 317 (2007) 790–792.
- [12] P. Preuster, C. Papp, P. Wasserscheid, Liquid organic hydrogen carriers (LOHCs): toward a hydrogen-free hydrogen economy, *Acc. Chem. Res.* 50 (2017) 74–85.
- [13] S. Zhang, Z. Xia, M. Zhang, Y. Zou, H. Shen, J. Li, X. Chen, Y. Qu, Boosting selective hydrogenation through hydrogen spillover on supported-metal catalysts at room temperature, *Appl. Catal. B Environ.* 297 (2021), 120418.
- [14] R. Yamaguchi, C. Ikeda, Y. Takahashi, Homogeneous catalytic system for reversible dehydrogenation-hydrogenation reactions of nitrogen heterocycles with reversible interconversion of catalytic species, *J. Am. Chem. Soc.* 131 (2009) 8410–8412.
- [15] W. Xue, H. Liu, B. Zhao, C. Tang, B.Y. Xia, B. You, Interheteromolecular hyperconjugation boosts (de)hydrogenation for reversible H<sub>2</sub> storage, *ChemSusChem* 16 (2023), e202201512.
- [16] L. Ge, M. Qiu, Y. Zhu, S. Yang, W. Li, X. Chen, Synergistic catalysis of Ru single-atoms and zeolite boosts high-efficiency hydrogen storage, *Appl. Catal. B Environ.* 319 (2022), 121958.
- [17] Y. Wu, H. Yu, X. Li, A rare earth hydride supported ruthenium catalyst for the hydrogenation of N-heterocycles: boosting the activity via a new hydrogen transfer path and controlling the stereoselectivity, *Chem. Sci.* 10 (2019) 10459–10465.
- [18] H. Chen, H. Shuang, W. Lin, X. Li, Z. Zhang, J. Fu, Tuning interfacial electronic properties of palladium oxide on vacancy-abundant carbon nitride for low-temperature dehydrogenation, *ACS Catal.* 11 (2021) 6193–6199.
- [19] Y. Dong, M. Yang, P. Int. J. Mei, Dehydrogenation kinetics study of perhydro-N-ethylcarbazole over a supported Pd catalyst for hydrogen storage application, *Hydrog. Energy* 41 (2016) 8498–8505.
- [20] D. Forberg, T. Schwob, R. Kempe, Single-catalyst high-weight% hydrogen storage in an N-heterocycle synthesized from lignin hydrogenolysis products and ammonia, *Nat. Commun.* 7 (2016) 13201.
- [21] T. Zhu, M. Yang, X. Chen, Y. Dong, Z. Zhang, H. Cheng, A highly active bifunctional Ru-Pd catalyst for hydrogenation and dehydrogenation of liquid organic hydrogen carriers, *J. Catal.* 378 (2019) 382–391.
- [22] W. Xue, H. Liu, B. Mao, H. Liu, M. Qiu, C. Yang, X. Chen, Y. Sun, Reversible hydrogenation and dehydrogenation of N-ethylcarbazole over bimetallic Pd-Rh catalyst for hydrogen storage, *Chem. Eng. J.* 421 (2020), 127781.
- [23] B. Chen, B. Hui, Y. Dong, Q. Sheng, X. Li, C. Liu, Distributions of Ni in MCM-41 for the hydrogenation of N-ethylcarbazole, *Fuel* 324 (2022), 124405.
- [24] B. Wang, P. Li, Q. Dong, L. Chen, H. Wang, T. Fang, Bimetallic NiCo/AC catalysts with a strong coupling effect for high-efficiency hydrogenation of N-ethylcarbazole, *ACS Appl. Energ. Mater.* 6 (2023) 1741–1752.
- [25] Y. Zhao, C. Li, Y. Zhu, L. Liu, T. Zhu, M. Yang, Controlled electron transfer at the Ni-ZnO interface for ultra-fast and stable hydrogenation of N-propylcarbazole, *Appl. Catal. B Environ.* (2023), 122792.
- [26] W. Xue, H. Liu, B. Zhao, L. Ge, S. Yang, X. Chen, Single Rh<sub>1</sub>Co catalyst enabling reversible hydrogenation and dehydrogenation of N-ethylcarbazole for hydrogen storage, *Appl. Catal. B Environ.* 327 (2023), 122453.
- [27] L. Ge, Y. Zhu, M. Qiu, S. Yang, N. Sun, W. Wei, X. Chen, A highly active Pd clusters hosted by magnesium hydroxide nanosheets promoting hydrogen storage, *Appl. Catal. B Environ.* 333 (2023), 122793.
- [28] H. Liu, C. Zhou, W. Li, W. Li, M. Qiu, Y. Sun, Ultralow Rh bimetallic catalysts with high catalytic activity for the hydrogenation of N-ethylcarbazole, *ACS Sustain. Chem. Eng.* 9 (2021) 5260–5267.
- [29] C. Li, M. Yang, Z. Liu, Z. Zhang, T. Zhu, X. Chen, H. Cheng, Ru-Ni/Al<sub>2</sub>O<sub>3</sub> bimetallic catalysts with high catalytic activity for N-propylcarbazole hydrogenation, *Catal. Sci. Tech.* 10 (2020) 2268–2276.
- [30] B. Wang, T. Chang, T. Fang, Component controlled synthesis of bimetallic PdCu nanoparticles supported on reduced graphene oxide for dehydrogenation of dodecahydro-N-ethylcarbazole, *Appl. Catal. B Environ.* 251 (2019) 261–272.
- [31] L. Kustov, A. Tarasov, O. Kirichenko, Microwave-activated dehydrogenation of perhydro-N-ethylcarbazole over bimetallic Pd-M/TiO<sub>2</sub> catalysts as the second stage of hydrogen storage in liquid substrates, *Int. J. Hydrog. Energ.* 42 (2017) 26723–26729.
- [32] A. Berkefeld, W. Piers, M. Parvez, Tandem frustrated lewis pair/tris (pentafluorophenyl)borane-catalyzed deoxygenative hydrosilylation of carbon dioxide, *J. Am. Chem. Soc.* 132 (2010) 10660–10661.
- [33] S. Liu, M. Dong, Y. Wu, S. Luan, Y. Xin, J. Du, S. Li, H. Liu, B. Han, Solid surface frustrated Lewis pair constructed on layered AlOOH for hydrogenation reaction, *Nat. Commun.* 13 (2022) 2320.
- [34] R. Dickerson, H. Gray, G. Haight, *Chemical Principles*, Benjamin/Cummings Publishing, 1979.
- [35] V. Muravev, G. Spezzati, Y. Su, A. Parastaev, F. Chiang, A. Longo, E. Hensen, Interface dynamics of Pd-CeO<sub>2</sub> single-atom catalysts during CO oxidation, *Nat. Catal.* 4 (2021) 469–478.
- [36] Q. Feng, S. Zhao, Y. Wang, J. Dong, W. Chen, D. He, Y. Li, Isolated single-atom Pd sites in intermetallic nanostructures: high catalytic selectivity for semihydrogenation of alkynes, *J. Am. Chem. Soc.* 139 (2017) 7294–7301.
- [37] H. Wang, Q. Luo, W. Liu, Y. Lin, Q. Guan, X. Zheng, J. Lu, Quasi Pd<sub>1</sub>Ni single-atom surface alloy catalyst enables hydrogenation of nitriles to secondary amines, *Nat. Commun.* 10 (2019) 4998.
- [38] S. Chen, B. Gong, J. Gu, Y. Lin, B. Yang, J. Lu, Dehydrogenation of ammonia borane by platinum-nickel dimers: regulation of heteroatom interspace boosts bifunctional synergetic catalysis, *Angew. Chem. Int. Ed.* 134 (2022), e202211919.
- [39] Y. Li, S. Zhang, W. Cheng, Y. Chen, D. Luan, S. Gao, X. Lou, Loading single-Ni atoms on assembled hollow N-Rich carbon plates for efficient CO<sub>2</sub> electroreduction, *Adv. Mater.* 34 (2022), 2105204.
- [40] S. Kelly, N. Yang, G. Mickelson, N. Greenlay, E. Karapetrova, W. Sinkler, S. Bare, Structural characterization of Ni-W hydrocracking catalysts using in situ EXAFS and HRTEM, *J. Catal.* 263 (2009) 16–33.
- [41] Z. Liu, F. Huang, M. Peng, Y. Chen, X. Cai, L. Wang, Z. Hu, X. Wen, N. Wang, D. Xiao, H. Jiang, H. Sun, H. Liu, D. Ma, Tuning the selectivity of catalytic nitriles hydrogenation by structure regulation in atomically dispersed Pd catalysts, *Nat. Commun.* 12 (2021) 6194.
- [42] S. Tasker, E. Standley, T. Jamison, Recent advances in homogeneous nickel catalysis, *Nature* 509 (2014) 299–309.
- [43] V. Chernyshev, V. Ananikov, Nickel and palladium catalysis: stronger demand than ever, *ACS Catal.* 12 (2022) 1180–1200.
- [44] X. Chen, G. Li, M. Gao, Y. Dong, M. Yang, H. Cheng, Wet-impregnated bimetallic Pd-Ni catalysts with enhanced activity for dehydrogenation of perhydro-N-propylcarbazole, *Int. J. Hydrog. Energ.* 45 (2020) 32168–32178.
- [45] M. Yang, Y. Dong, S. Fei, H. Ke, H.A. Cheng, Comparative study of catalytic dehydrogenation of perhydro-N-ethylcarbazole over noble metal catalysts, *Int. J. Hydrog. Energ.* 39 (2014) 18976–18983.
- [46] F. Besenbacher, I. Chorkendorff, B. Clausen, B. Hammer, A. Molenbroek, J. Nørskov, I. Stensgaard, Design of a surface alloy catalyst for steam reforming, *Science* 279 (1998) 1913–1915.
- [47] L. Kibler, A. El-Aziz, R. Hoyer, D. Kolb, Tuning reaction rates by lateral strain in a palladium monolayer, *Angew. Chem. Int. Ed.* 44 (2005) 2080–2084.